

DOI: 10.1002/ ((please add manuscript number))

## Boosting Efficient and Sustainable Alkaline Water Oxidation on W-CoOOH-TT Pair Sites Catalyst Synthesized via Topochemical Transformation

Ligang Wang, Hui Su, Guoying Tan, Junjie Xin, Xiaoge Wang, Zhuang Zhang, Yaping Li, Yi Qiu, Xiaohui Li, Haisheng Li, Jing Ju, Xinxuan Duan, Hai Xiao, Wenxing Chen, Qinghua Liu\*, Xiaoming Sun\*, Dingsheng Wang and Junliang Sun\*

Dr. L. G. Wang, J. J. Xin, X. G. Wang, Y. Qiu, Dr. X. H. Li, H. S. Li, J. Ju, Prof. J. L. Sun

College of Chemistry and Molecular Engineering, Peking University, Beijing National Laboratory for Molecular Sciences (BNLMS), 5 Yiheyuan Road, Beijing 100871, China. E-mail: junliang.sun@pku.edu.cn

Dr. H. Su

Key Laboratory of Light Energy Conversion Materials of Hunan Province College, College of Chemistry and Chemical Engineering, Hunan Normal University, Changsha 410081, China.

G. Y. Tan, Z. Zhang, Y. P. Li, X. X. Duan, Prof. X. M. Sun

State Key Laboratory of Chemical Resource Engineering, and Beijing Advanced Innovation Centre for Soft Matter Science and Engineering, Beijing University of Chemical Technology, Beijing 100029, China. E-mail: sunxm@mail.buct.edu.cn

Dr. L. G. Wang, Prof. H. Xiao, Prof. D. S. Wang

Department of Chemistry, Tsinghua University, Beijing 100084, China.

This article has been accepted for publication and undergone full peer review but has not been through the copyediting, typesetting, pagination and proofreading process, which may lead to differences between this version and the [Version of Record](#). Please cite this article as [doi: 10.1002/adma.202302642](#).

This article is protected by copyright. All rights reserved.

Prof. Q. H. Liu

National Synchrotron Radiation Laboratory, University of Science and Technology of China, Hefei 230029, Anhui, China. E-mail: qhliu@ustc.edu.cn

Dr. W. X. Chen

Energy & Catalysis Center, School of Materials Science and Engineering, Beijing Institute of Technology, Beijing 100081, China.

**Keywords:** pair sites catalysts, topochemical transformation, oxygen evolution reaction, in situ XAFS, high current density

## Abstract

The development of facile methods for constructing highly active, cost-effective catalysts that meet ampere-level current density and durability requirements for an oxygen evolution reaction is crucial. Herein, we posit a general topochemical transformation strategy: the M-Co<sub>9</sub>S<sub>8</sub> single atom catalysts (SACs) are directly converted into M-CoOOH-TT (M = W, Mo, Mn, V) pair sites catalysts under the role of incorporating of atomically dispersed high valence metals modulators through potential cycling. Furthermore, in situ X-ray absorption fine structure spectroscopy was used to track the dynamic topochemical transformation process at the atomic level. The W-Co<sub>9</sub>S<sub>8</sub> breaks through the low overpotential of 160 mV at 10 mA cm<sup>-2</sup>. A series of pair-site catalysts exhibit a large current density approaching 1,760 mA cm<sup>-2</sup> at 1.68 V vs. RHE in alkaline water oxidation and achieve a ~240-fold enhancement in the normalized intrinsic activity compared to that reported CoOOH, and sustainable stability of 1,000 h. Moreover, we confirmed the O–O bond formation via a two-site

mechanism, supported by in situ synchrotron radiation infrared and DFT simulations, which breaks the limit of adsorption–energy scaling relationship on conventional single-site.

## 1. Introduction

With concerns about global climate warming and the growing energy shortage crisis caused by the massive use of fossil fuels, tremendous efforts have been focused on exploiting and utilizing zero-emission, clean-fuel, and sustainable energy sources.<sup>[1, 2]</sup> Inspired by natural and artificial photosynthetic energy conversion, an efficient technology for splitting water into H<sub>2</sub> and O<sub>2</sub> could provide sustainable energy production to meet the increasing global energy demands and ensure a cleaner environment.<sup>[3]</sup> In water splitting, the electrochemical oxygen evolution reaction (OER) is a significant step for obtaining both hydrogen energy and photosystem II (PSII). Moreover, the low energy-utilization efficiency and low output power are common issues, which are ascribed to high energy barriers and sluggish kinetics involving multiple oxygen intermediates with two steps of O–H bond breaking and subsequent O–O bond formation.<sup>[4-6]</sup> Inspired by nature's oxygen-evolving complex (OEC), many multi-nuclear transition metal complexes, such as cobalt-tungsten-based compounds ([Co<sub>4</sub>(H<sub>2</sub>O)<sub>2</sub>(PW<sub>9</sub>O<sub>34</sub>)<sub>2</sub>]),<sup>[7, 8]</sup> have been successfully prepared and have demonstrated high activity in the OER. Furthermore, it has been claimed that multinuclear metal active sites play a vital role in accelerating oxygen–oxygen coupling and promoting O–O bonding in the OER. Sargent et al. reported homogeneously dispersed FeCoW oxygen-evolving catalysts that exhibited an excellent OER performance via a dual-site mechanism, which was mainly ascribed to the overcoming of the thermodynamically limiting process with Co<sup>3+</sup>/Co<sup>4+</sup> oxidation cycling via high-valence W<sup>6+</sup>-species modulating Co-based oxyhydroxides.<sup>[9, 10]</sup> This provides valuable experience in designing efficient

WCo-based catalysts from an atomic-level perspective to meet the actual requirement of high current density at a lower applied bias.

Recently, eco-friendly and earth-abundant supports provided atomically dispersed catalysts with highly uniform atomic scale dispersion and maximum atom utilization and an excellent catalytic performance, thus providing a highly desirable platform for catalysis research.<sup>[11-14]</sup> It has been confirmed that catalytic activity and stability can be optimized by tuning the local electronic structure and structural reconstruction of supports based on strong metal-support interactions (SMSI).<sup>[15-17]</sup> Among the various supports, transition metal dichalcogenides (TMDs) usually derived highly active catalytic sites for OER because of the unique adjustability of their electronic structure and the coordination environment with the presence of SMSI. Some reports have demonstrated that cobalt sulfides ( $\text{CoS}_x$ ) usually underwent topochemical self-reconstruction to derive highly stable cobalt oxyhydroxides ( $\text{CoOOH}$ ) sites that contributed to superior OER during potential cycling.<sup>[18, 19]</sup> However, there are no reports on the rapid topological transformation of cobalt sulfide supports for forming stable  $\text{CoOOH}$  by modulating high-valence single-atom metals via potential cycling.

Herein, we used in situ X-ray absorption fine structure spectroscopy (XAFS) to track the dynamic structural reconstruction of  $\text{Co}_9\text{S}_8$  to  $\text{CoOOH}$  and obtained a deeper insight into the underlying mechanism of high-valence metal-induced topological transformation under potential cycling. A general potential cycling topochemical transformation (PCTT) strategy of directly converting  $\text{M-Co}_9\text{S}_8$  single atom catalysts (SACs) into  $\text{M-CoOOH-TT}$  pair sites ( $\text{M} = \text{W}, \text{Mo}, \text{Mn}, \text{and V}$ ) catalysts with the help of atomically dispersed high-valence metals was firstly identified, which was different from the reported topochemical transformation process.<sup>[20, 21]</sup> Furthermore, the unique pair sites catalysts with strong electronic coupling between dual metal sites and an atomically dispersed metal site

comparable to that of SACs, which endowed the local electric field to optimize the binding energy and accelerate the kinetic process of oxygen-containing species.<sup>[22-24]</sup> Moreover, a series of WCo-based pair sites delivered breakthrough results: enhanced catalytic activity (450 mV at a high current density of 1,760 mA cm<sup>-2</sup>), superior durability (continuous operation for 1,000 h), and superior normalized intrinsic activity towards oxygen evolution. The restructured W-CoOOH-TT pair-site catalyst with a suitable Co-Co active site distance was favorable for the conversion of oxygenates via the formation of oxygen bridges, especially for the binding of \*OH at the double cobalt site, further deprotonation, and the realization of oxygen–oxygen coupling to O–O bond formation, which suggests the occurrence of a the two-site mechanism for the OER rather than a conventional single-site adsorbate evolution mechanism (AEM).<sup>[9, 25, 26]</sup> Although a two-site mechanism has been proposed in a few studies,<sup>[9, 27-30]</sup> the majority of them were only the results of DFT theoretical studies, which are limited by difficulties in realizing the real-time and efficient in situ detection of adsorption and conversion in oxygenates in experiments. Building on previous research,<sup>[9, 26, 31-35]</sup> we identified a favorable direct O–O radical coupling oxide path mechanism (OPM)-type for two-site O<sub>2</sub> evolution that involved typical forming oxygen bridges between metal Co sites with a distinctive absorption peak at 1,078 cm<sup>-1</sup> via in situ synchrotron radiation Fourier transform infrared (SR-FTIR) and DFT simulations. This was similar to the reported intramolecular oxygen coupling (I2M) but not water hydrogen atom abstraction (WHAA) mechanisms of the PSII, obviously inconsistent with the conventional single-site OER mechanism.<sup>[9, 25, 30]</sup>

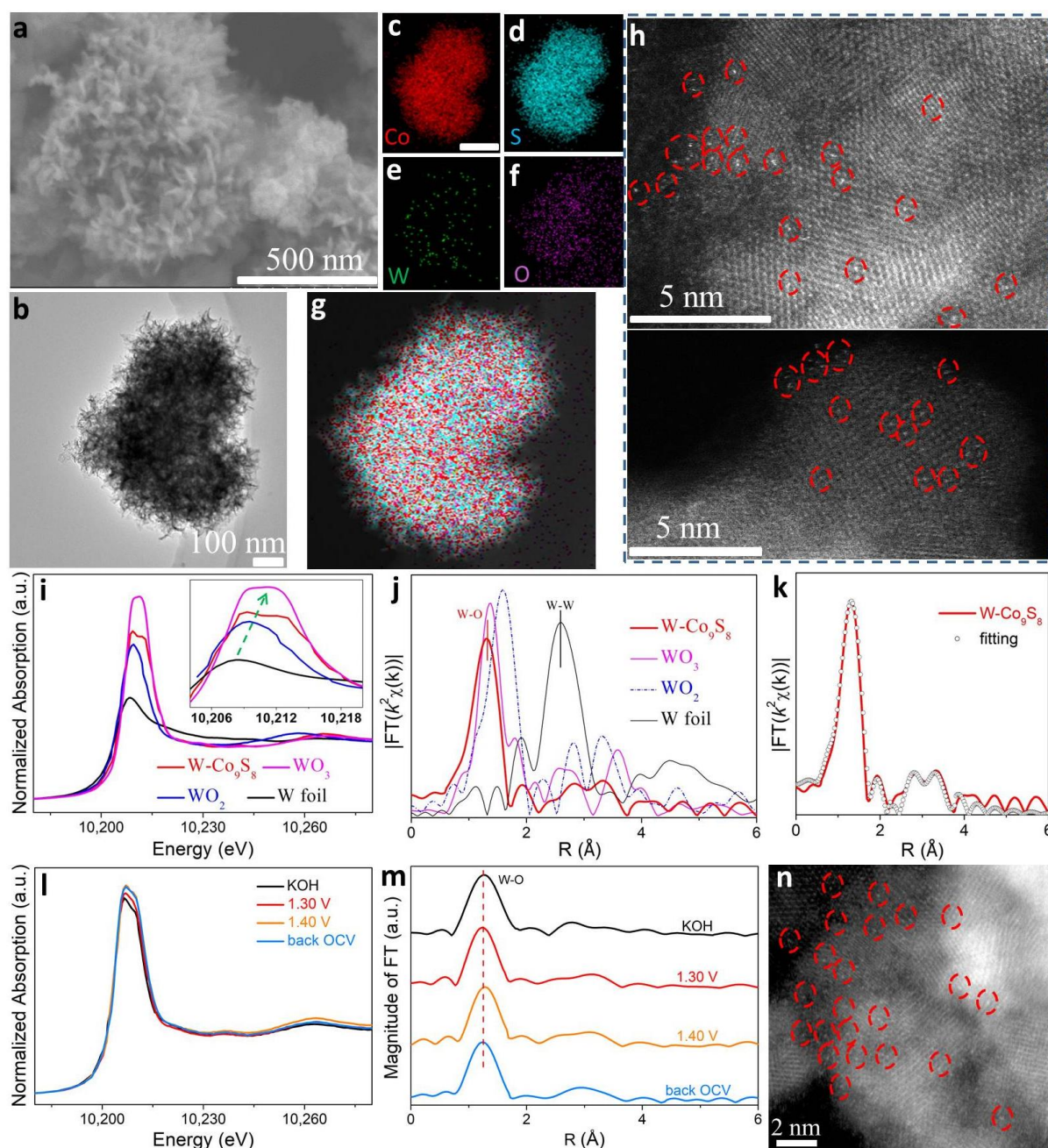


**Figure 1.** Morphology, structural characterization and in situ XAFS of the W-Co<sub>9</sub>S<sub>8</sub> SACs. a-g) Electron microscope analysis of the W-Co<sub>9</sub>S<sub>8</sub> SACs: a) SEM and b) TEM images of W-Co<sub>9</sub>S<sub>8</sub>. c-g) The HAADF-STEM elemental mapping and corresponding elemental distribution maps of Co, W, S and O in the W-Co<sub>9</sub>S<sub>8</sub>. h) Aberration-corrected HAADF-STEM images in different regions (some of the isolated tungsten atoms are marked with red circles). i) The experimental  $L_3$ -edge XANES spectra of W-Co<sub>9</sub>S<sub>8</sub> catalyst and reference samples (WO<sub>3</sub>, WO<sub>2</sub> and W foil), the inset expresses the partially enlarged data. j) Fourier transforms (FTs) of the W  $L_3$ -edge EXAFS oscillations of W-Co<sub>9</sub>S<sub>8</sub>, WO<sub>3</sub>, WO<sub>2</sub> and W foil samples. k) The fitting curves of  $k^2$ -

This article is protected by copyright. All rights reserved.

weighted EXAFS spectra of W-Co<sub>9</sub>S<sub>8</sub>. l,m) In situ W *L*<sub>3</sub>-edge XANES spectra and the corresponding Fourier-transformed *k*<sup>2</sup>-weighted EXAFS signals of W-Co<sub>9</sub>S<sub>8</sub> recorded under different applied potential cycling. n) The AC HAADF-STEM images of W-Co<sub>9</sub>S<sub>8</sub> after 30 cyclic voltammetry (CV) cycles. The red circles was used to mark the W single sites.

## 2. Results and discussion

**Discovery and elucidation of topological transformation mechanism using in situ XAFS.** In the experiments, we first used a continuous two-step solvothermal synthesis strategy to construct Co<sub>9</sub>S<sub>8</sub>-supported single-atomic-site tungsten catalysts and dried them in vacuum, after which, the W-Co<sub>9</sub>S<sub>8</sub> SACs powder samples were acquired (see Methods, Supporting Information). Scanning electron microscopy (SEM) images revealed that W-Co<sub>9</sub>S<sub>8</sub> exhibited a peony-like hierarchical structure consisting of highly porous ~20-nm thick nanosheet arrays (Figure 1a, and Figure S1, Supporting Information). The measured specific Brunauer-Emmett-Teller (BET) surface area of W-Co<sub>9</sub>S<sub>8</sub> was ~71.2 m<sup>2</sup> g<sup>-1</sup> (Figure S2, Supporting Information), which was approximately five to seventeen times greater than those of bare Co<sub>9</sub>S<sub>8</sub> and previously reported metal-oxide materials.<sup>[36]</sup> The transmission electron microscopy (TEM) and high-resolution TEM (HRTEM) images indicated that W-Co<sub>9</sub>S<sub>8</sub> comprised numerous wrinkled and thin nanoflakes (Figure 1b, Figure S3, Supporting Information). The corresponding energy-dispersive spectroscopy (EDS) elemental mapping results of Co, W, S and O correspond well to those profiles of W-Co<sub>9</sub>S<sub>8</sub> nanoflakes in Figure 1c–g and Figure S4 (Supporting Information), which preliminarily indicates that the isolated W atoms were uniformly dispersed throughout the Co<sub>9</sub>S<sub>8</sub> support, with a tungsten concentration of ~0.92 wt.%. This result was consistent with the inductively coupled plasma-atomic emission spectrometer (ICP-AES) analysis (0.95 wt.%) (Table S1, Supporting Information). It should be noted that bright spots (with the sizes ~2 Å) were observed in an aberration-corrected high-angle annular dark-field scanning transmission electron microscopy (AC HAADF-STEM) image, as shown in Figure 1h, thus further indicating the

formation of atomic dispersion W sites over the  $\text{Co}_9\text{S}_8$  support. Correspondingly, the powder X-ray diffraction (PXRD) patterns were also in accordance with this phenomenon, without the presence of any visible nanoparticles/clusters in both the low- and high-magnification TEM images. The Rietveld refinement analysis of the PXRD indicated that the synthesized  $\text{W-Co}_9\text{S}_8$  was consistent with the space group of pure  $\text{Co}_9\text{S}_8$  ( $Fm\bar{3}m$ ), and the final refinement converged to  $R_{\text{wp}} = 1.31\%$  and  $R_p = 0.91\%$  (Figures S5 and S6 and Table S2, Supporting Information). The refinement results revealed that the structure of single-atom sites W loaded  $\text{Co}_9\text{S}_8$  exhibited almost no change and coincided well with the premier cubic structure of  $\text{Co}_9\text{S}_8$  crystals.

The high-resolution X-ray photoelectron spectroscopy (XPS) spectra of the W 4f binding energies in the  $\text{W-Co}_9\text{S}_8$  SACs displayed the two independent peaks of 35.6 and 37.7 eV, respectively, which shifted to higher values and were close to  $\text{WO}_3$ , thus indicating the existence of oxidized  $\text{W}^{6+}$  species compared to the lower oxidation state of  $\text{WS}_2$  or  $\text{WO}_2$  (Figure S7 and Table S3, Supporting Information). The normalized W  $L_3$ -edge X-ray absorption near-edge spectroscopy (XANES) results demonstrated that the intensities of the  $\text{W-Co}_9\text{S}_8$ ,  $\text{WO}_3$ , and  $\text{WO}_2$  prominent peaks were higher than that of the W foil (Figure 1i), suggesting the oxidized electronic structure of W in  $\text{W-Co}_9\text{S}_8$ . Furthermore, the intensities of the white lines of  $\text{W-Co}_9\text{S}_8$  (10,210.11 eV) were higher than that of  $\text{WO}_2$  (10,209.59 eV) and very close to that of  $\text{WO}_3$  (10,210.75 eV), as shown in the inset of Figure 1i, which reveals the dominance of  $\text{W}^{6+}$  in  $\text{W-Co}_9\text{S}_8$ . These results agree with the above XPS results. Typically, the extended XAFS (EXAFS) spectra of the W foil exhibited a dominant peak at 2.60 Å, corresponding to W–W coordination. The Fourier transform EXAFS (FT-EXAFS) spectra in Figure 1j exhibited W  $L_3$ -edge EXAFS oscillations of the relevant materials, wherein the W–W contribution to the W foil was absent for  $\text{W-Co}_9\text{S}_8$ , which strongly indicates that there were no W particles or



clusters in W-Co<sub>9</sub>S<sub>8</sub>. Furthermore, the sample in the R space of W-Co<sub>9</sub>S<sub>8</sub> (Figure 1j) only exhibited one sharp peak located at approximately 1.40 Å, which can be ascribed to the W–O coordination of the reference WO<sub>3</sub> and reported single-atom tungsten.<sup>[37, 38]</sup> One visible migration of the W–O peak (1.33 Å) for W-Co<sub>9</sub>S<sub>8</sub> can be observed in comparison with WO<sub>3</sub> (1.36 Å) and WO<sub>2</sub> (1.59 Å), indicating the different W–O environment in the atomically dispersed W condition. Furthermore, the FT-EXAFS and k-space fitting of W-Co<sub>9</sub>S<sub>8</sub> while considering Co-W scattering (Figure 1k, and Figure S8 and Table S4, Supporting Information) indicated that W atoms were coordinated to O atoms from the partial oxidation of the ostensible sulfur species. Moreover, no obvious peak was observed at approximately 2.20 Å, suggesting that no W–S bond formed in W-Co<sub>9</sub>S<sub>8</sub> according to the literature.<sup>[39]</sup> Collectively, these observations provide solid evidence for verifying the successful formation of the W-Co<sub>9</sub>S<sub>8</sub> sample with Co<sub>9</sub>S<sub>8</sub> supported atomically dispersed W sites.

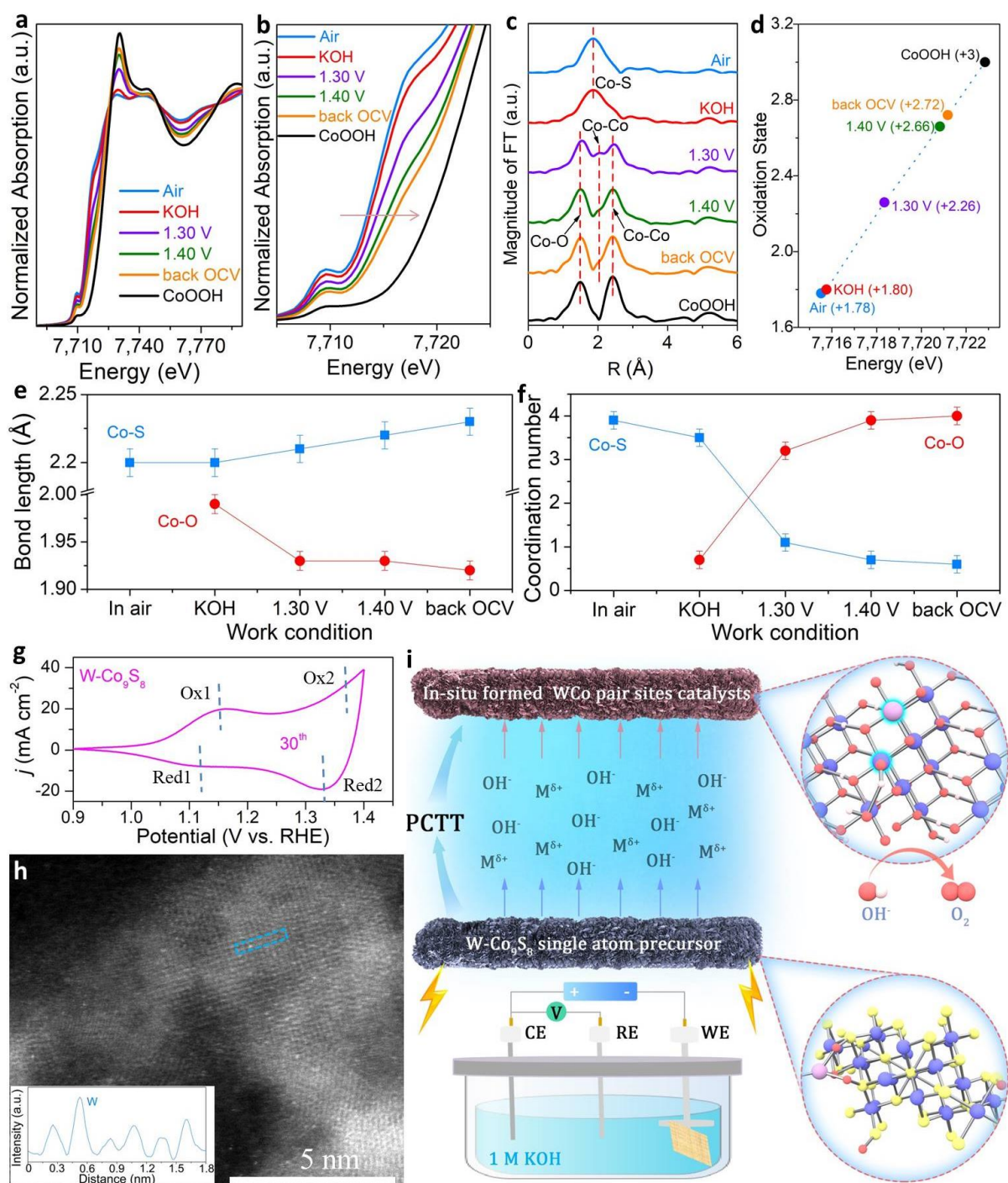


**Figure 2.** In situ XAFS to track the topochemical transformation during potential-driven cycles. a-c) In situ Co K-edge XANES and the Fourier-transformed  $k^3$ -weighted EXAFS spectra of W-Co<sub>9</sub>S<sub>8</sub> with structural topochemical transformation under potential cycling. d) Linear fitting average chemical valence of Co from XANES spectra. e-f) The fitted change parameters of bond length and coordination number for the

Co-O and Co-S coordination shells. Error bars in (e,f) are deduced by the least-square curve fit method and stand for standard deviation. g) The 30<sup>th</sup> CVs of W-Co<sub>9</sub>S<sub>8</sub> SACs. h) The AC HAADF-STEM image for W-CoOOH-TT pair sites catalyst. The inset in (h) showed the corresponding intensity profile marked by the blue dashed box. i) Topochemical transformation process from the SCAs precursor to the W-CoOOH-TT pair sites catalysts by potential-cycling self-reconstruction. It should be noted that WCo represents W-CoOOH-TT.

To further study the topochemical transformation process from W-Co<sub>9</sub>S<sub>8</sub> SACs to W-Co<sub>9</sub>S<sub>8</sub>-TT and W-CoOOH-TT pair sites catalysts, and to elucidate the dynamic evolution of the geometric and electronic states during the electrochemical cycles, in situ XAFS measurements, including XANES and EXAFS analyses, were performed. During in situ XANES measurement, the W-Co<sub>9</sub>S<sub>8</sub> SACs had undergone various environments from air to alkaline electrolyte to the presence of applied bias. The potential was first increased from 1.30 to 1.40 V vs. RHE and was then returned to the open-circuit voltage (denoted as OCV). In the case of W, Figure 1l and Figure S9 (Supporting Information) demonstrated an obvious positive shift in the normalized in situ W *L*<sub>3</sub>-edge XANES when the applied potential was gradually increased to 1.40 V vs. RHE, thus indicating that W was oxidized to a higher oxidation state during the OER. To explore the local structural changes in addition to the valence states, we conducted in situ EXAFS measurements. The corresponding main peak of the W *L*<sub>3</sub>-edge FT-EXAFS spectra exhibited an almost constant radial distance, indicating an unchanged local atomic structure (Figure 1m). The structural changes parameters, such as bond length and coordination number (CN), were inferred by data fitting in R considering Co-W scattering and the  $Re(k^3\chi(k))$  oscillations (Figures S10-S13 and Table S5, Supporting Information). Furthermore, the EXAFS and AC HAADF-STEM suggested that the W species always existed as isolated single atomic sites without probable agglomeration (Figure 1m and 1n), indicating good topochemical transformation stability during potential cycling.

Based on the potential-driven structural variability of cobalt sulfide in alkaline medium, we used in situ XAFS to reveal the topological conversion process. The Co XANES absorption spectra of W-Co<sub>9</sub>S<sub>8</sub> SACs shed light on an apparent shift to higher energy when the applied potential increased to 1.40 V vs. RHE, indicating the oxidation process of the Co species (Figure 2a and 2b). Combining the structure evolution with OER cycle, we divided the topochemical conversion process from Co<sub>9</sub>S<sub>8</sub> to CoOOH into four stages: the resting state from air to KOH solution (stage “1”), the pre-catalytic state from unbiased to 1.30 V vs. RHE (stage “2”), the catalytic state from 1.30 V to 1.40 V vs. RHE (stage “3”) and the catalyst repair state from 1.40 V vs. RHE coming back to OCV (stage “4”). When switching from stage “1” to “2” with lasting one hour, the intensity of the main Co XANES absorption peak at 7,730 eV at 1.30 V vs. RHE increased obviously compared with the pristine sample without applied potential. Correspondingly, the main peak in the FT-EXAFS spectra displayed a visible change with the disappearance of the cobalt-sulfur bond, accompanied by the appearance of the cobalt-oxygen bond (Figure 2c). As its name implies, the topochemical structural transformation occurred from Co<sub>9</sub>S<sub>8</sub> to cobalt (oxy)hydroxides (CoOOH), following the obviously enhanced oxygen signal through STEM-EDS mapping (Figure S14, Supporting Information). Following an applied potential larger than 1.30 V (stage “3”), the most obvious feature was that the Co *K*-edge XANES peaks gradually shifted to higher energy (Figure 2b), suggesting an increase in Co oxidation state. The structural features of the Co-O bond derived from the W-Co<sub>9</sub>S<sub>8</sub> SACs were very similar to those of the cobalt oxygen bond in the reference CoOOH,<sup>[40]</sup> implying a successive potential-driven topochemical transformation process. The FT-EXAFS spectra (Figure 2c) exhibited obvious peaks for Co–O distances at ~1.50 Å (phase uncorrected) in a range of 1.30 V to back OCV and typical contributions from relatively distant coordination shells between 2.40–2.45 Å (phase uncorrected), mainly was ascribed to di-μ-

oxo bridged Co ions.<sup>[41, 42]</sup> By comparing the in situ XAFS results of W-Co<sub>9</sub>S<sub>8</sub> SACs and Co<sub>9</sub>S<sub>8</sub> (Figure 2c, Figure S15 in Supporting Information), it can be found that the presence of single-atom W can facilitate the topochemical transformation of Co<sub>9</sub>S<sub>8</sub> to highly stable CoOOH at a lower voltage ( ~ 1.30 V vs. RHE), while the pure Co<sub>9</sub>S<sub>8</sub> catalyst required a higher potentials ( $\geq 1.50$  V vs. RHE) to achieve structural topological transformation. Additionally, the increased Co oxidation state provided solid evidence of the transformation from Co<sub>9</sub>S<sub>8</sub> to CoOOH during the OER cycling (Figure 2d). The fitted average oxidation states accurately indicated the obvious increasing trend from +1.78 to +2.26, and +2.66 for the catalyst under the air condition, +1.30 and +1.40 V vs. RHE, respectively. Especially, the cobalt valence state cannot be returned to its original form and the Co<sub>9</sub>S<sub>8</sub> species experienced an irreversible self-optimization topological transformation during potential-cycling (stage “4”), when the potential restored back to OCV, inferring that the irreversibility in the Co oxidation state. Structural change parameters, such as the bond length and coordination number (CN), were inferred via data fitting in R and the  $Re(k^3\chi(k))$  oscillations of different fitting paths (Figure 2e and 2f, and Figures S16–S20 and Table S6, Supporting Information). The fitting results revealed that the bond length distance of Co–O decreased slightly from 1.99 to 1.92 Å along with an apparent increase in CN from 1.0 to 4.0 under the promoting potential. This decrease was consistent with the reported results that the Co–O bond distance in CoOOH was shorter than that in Co(OH)<sub>2</sub>.<sup>[9]</sup> However, the opposite situation for Co–S was observed with an increasing bond distance from 2.20 to 2.23 Å and obvious reduced CN. This demonstrates that the stronger Co–O interaction as the potential increased presented a higher oxidation state and a more enhanced charge transfer via the SMSI effect, which caused the cobalt–sulfur bond to become stretched and elongated and the cobalt–oxygen bond to become shortened. Noting that the W-CoOOH-TT derived from W-Co<sub>9</sub>S<sub>8</sub> exhibited a

lower Co valence state and CN of Co–O compared to the bulk CoOOH phase. The above in situ XAFS results for W and Co fully confirmed that Co<sub>9</sub>S<sub>8</sub> underwent a topological transformation process to form a CoOOH structure, and tungsten always maintained atomic-level dispersion.

It should be noted that the characteristic peak of the cyclic voltammetry (CV) curve obtained during cycling was also helpful in revealing the structural topochemical transformation of cobalt sulfide to CoOOH. Previous studies have demonstrated the significance of the pre-oxidation of Co species for water oxidation, wherein Co<sup>2+</sup> tended to become easily oxidized to Co<sup>3+</sup> or a higher oxidation state with an increase in voltage.<sup>[43-45]</sup> Usually, the obtained high-valence Co(oxyhydr)oxide was considered a highly stable active site for the OER. For the W-Co<sub>9</sub>S<sub>8</sub> SACs, the CV results exhibited negligible changes during continuous cycles from the 30<sup>th</sup> to the 100<sup>th</sup> cycle (Figure S21, Supporting Information). The CV of the W-Co<sub>9</sub>S<sub>8</sub> SACs appeared two broad redox transitions with an oxidation peak (Ox1) at ~1.15 V vs. RHE and a reduction peak (Red1) at ~1.10 V vs. RHE and (Ox2-Red2) at ~1.35 VRHE (Figure 2g). The obvious redox transition waves at approximately 1.10 V vs. RHE were commonly attributed to the Co<sup>2+</sup>/Co<sup>3+</sup> redox couples. The oxidation peak (Ox2) coincided with the onset of the OER and resulted from the charge redistribution in the Co–O\* ligand environment. Furthermore, the obvious pair of redox peak feature curves at 30<sup>th</sup> were consistent with the characteristic polarization curve of the reported CoOOH.<sup>[41, 46-48]</sup> This electrochemical feature revealed that the W-Co<sub>9</sub>S<sub>8</sub> SACs may experience an irreversible self-reconstruction topological transformation into oxyhydroxide. Furthermore, the cathodic peaks both in the 30<sup>th</sup> and 100<sup>th</sup> cycles appeared at ~1.10 V and ~1.32 V for restructuring the W-Co<sub>9</sub>S<sub>8</sub>-TT, while an obvious right-shift cathodic peak was observed for CoOOH (~1.18 and 1.50 V).<sup>[41, 46, 47]</sup> No obvious redox characteristic peaks of CoOOH were observed for Co<sub>9</sub>S<sub>8</sub> during the continuous cycles (Figure S22, Supporting

Information), which was also consistent with the in situ XAFS results; that is, it was difficult to achieve the topological transformation of the pure samples at potentials lower than 1.40 V. The in situ XAFS described above further revealed the structural evolution from  $\text{Co}_9\text{S}_8$  to  $\text{CoOOH}$  via potential-driven cycling, which was also consistent with recent reports.<sup>[49]</sup>

Considering the above in situ XAFS and CV results, we proposed a straightforward view that the evolution process of the species undergoes a continuous topological transformation:  $\text{Co}_9\text{S}_8 \rightarrow \text{Co}(\text{OH})_2 \rightarrow \text{CoOOH}$ .<sup>[50, 51]</sup> Considering the strong SMSI in the SACs with supports, the accelerated structural oxidation process of  $\text{Co}_9\text{S}_8$  to  $\text{CoOOH}$  was mainly attributed to the charge transfer between  $\text{Co}_9\text{S}_8$  and high-valence W at the interfacial region and the increasing potential. Furthermore, we concluded that the preferred structural  $\text{CoOOH}$  species were composed of di- $\mu$ -oxo-bridged Co ions containing a favorable coordination environment, which is consistent with previous reports.<sup>[41, 52]</sup> When high-valence W single atoms were loaded, the interaction between the high-valence metal and the support promoted the formation of an oxygen bridge bond with Co (labeled W–O–Co), and further topology reconstruction could be achieved at lower potentials compared with pure  $\text{Co}_9\text{S}_8$ . Moreover, a W- $\text{CoOOH}$ -TT pair sites catalyst with atomically dispersed W can be successfully prepared through topochemical transformation by potential cycle driving (Figure 2h). This dynamic “dissolution–redeposition” change can be visually described as “PCTT” with the assistance of high-valence metal SACs, as shown in Figure 2i.<sup>[53]</sup> The “PCTT” process generally included the following three steps: 1) degradation of surface  $\text{Co}_9\text{S}_8$  precursor and cationic dissolution induced by oxidation of surface sulfide under the application of potential cycling and high-valence SACs; 2) re-deposition of dissolved cations reacting with  $\text{OH}^-$  in the electrolyte; and 3) formation of a

new phase through topological transformation. Meanwhile, the migration and exchange of metal ions usually also occurred in the above topochemical transformation.<sup>[54]</sup>

**Evaluation of electrocatalytic water oxidation activity.** We first focused on the evaluation of the OER performance of the working electrodes in a three-electrode configuration at room temperature. The W-Co<sub>9</sub>S<sub>8</sub> SACs required a small overpotential of 160 mV to obtain 10 mA cm<sup>-2</sup> and had a low Tafel slope of 32 mV dec<sup>-1</sup>, which even exceeded that of the noble metal oxides IrO<sub>2</sub> and RuO<sub>2</sub> (Figure 3a; Figures S23–S25 and Table S7, Supporting Information). Furthermore, the CV curves indicated that the W-Co<sub>9</sub>S<sub>8</sub>-TT pair sites exhibited remarkable OER activity, with an overpotential of 246 mV to obtain a current density of 10 mA cm<sup>-2</sup> and an extremely small Tafel slope of 21 mV dec<sup>-1</sup> (Figure 3b and Figure S26, Supporting Information). In addition to the low overpotential demand, the long-term stability was another critical parameter for realizing a practical OER electrode. Therefore, we further adopted the “PCTT” strategy to fabricate a W-CoOOH-TT pair sites catalyst by potential cycling the W-Co<sub>9</sub>S<sub>8</sub> precursor. In this process, the catalyst underwent a structural topological transformation and evolved from unstable W-Co<sub>9</sub>S<sub>8</sub> and W-Co<sub>9</sub>S<sub>8</sub>-TT structures to a robust W-CoOOH-TT pair sites catalyst. Furthermore, a series of characterization techniques such as XPS, PXRD, and HRTEM and corresponding mapping systematically indicated that Co<sub>9</sub>S<sub>8</sub> can be almost completely be converted to CoOOH within 900 segments of cycling using the CV technology (Figures S27–S33, Supporting Information), which was consistent with the previously reported experimental results.<sup>[18, 50, 51]</sup>



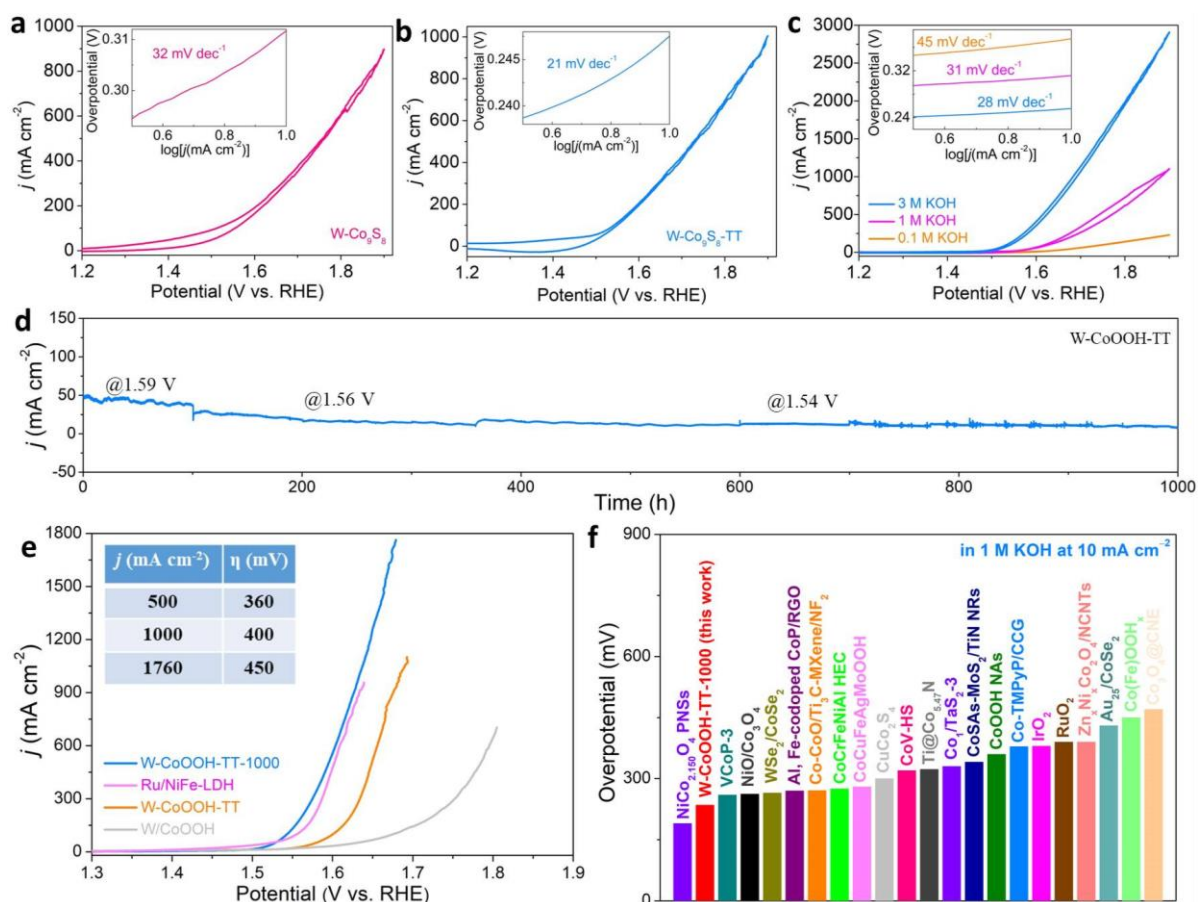


**Figure 3.** Electrochemical OER activity. a-c) The CV of W-Co<sub>9</sub>S<sub>8</sub> SACs (a), W-Co<sub>9</sub>S<sub>8</sub>-TT pair sites (b), W-CoOOH-TT pair sites catalysts (c) measured with a 5 mV s<sup>-1</sup> scan rate in 1.0 M KOH. Insets: the obtained corresponding Tafel slopes from backward scanning. d) The current density versus time (*i-t*) curves of W-CoOOH-TT pair sites catalysts recorded for total 1000 h at various potentials vs. RHE. Noting that the durability evaluation via *i-t* test at constant potential of 1.59, 1.56 and 1.54 V vs. RHE for 100, 260 and 640 h, respectively. e) The OER polarization curves with *iR* compensation. Insets: the W-CoOOH-TT-1000 exhibited current density at specific potential. f) Comparison of the overpotential of W-CoOOH-TT-1000 and recently reported Co-based OER electrocatalysts at 10 mA cm<sup>-2</sup> in 1 M KOH. The overpotential of W-CoOOH-TT-1000 were determined from polarization curves obtained at a scan rate of 5 mV s<sup>-1</sup> and other values were plotted from references in Table S8 for (f), respectively.

As expected, the W-CoOOH-TT pair sites exhibited an excellent OER activity of 1000 and 2890 mA cm<sup>-2</sup> ultra-high current density at a lower overpotential of 450 and 670 mV (Figure 3c and Figures S34 and S35, Supporting Information), respectively, under 3 M KOH. Correspondingly, the W-

CoOOH-TT exhibited the fastest kinetics with the lowest Tafel slope of 28 mV dec<sup>-1</sup> in 3 M KOH (inset of Figure 3c and Figure S36, Supporting Information), which was lower than that of 45 mV dec<sup>-1</sup> (0.1 M KOH). In addition, the Tafel slope of 31 mV dec<sup>-1</sup> for the W-CoOOH-TT pair sites catalyst was in agreement with the results of the O–O bond formation in the OPM-type OER mechanism (inset of Figure 3c).<sup>[26]</sup> Moreover, the durability of the W-CoOOH-TT pair sites in the OER was studied by performing *i*–*t* measurements for a continuous 1,000 h at various constant potentials with almost unchanged current densities, which was superior to that of the noble metal IrO<sub>2</sub> with a significant loss (Figure 3d and Figure S37, Supporting Information). After 1,000 h, the W-CoOOH-TT pair sites catalysts exhibited an increased polarization current curve in comparison to the initial one (Figures S38 and S39, Supporting Information). Surprisingly, the AC HAADF-STEM images demonstrated that W-CoOOH-TT with atomically dispersed tungsten species could better maintain its state during the long-term alkaline OER cycle process (Figure S40, Supporting Information). In addition, the XPS and SEM results for the W-CoOOH-TT pair sites catalysts after 1,000 h of OER running further indicated that the structure and hierarchical morphology were almost unchanged in comparison with the initial conditions (Figures S41–S43, Supporting Information), thus suggesting a superior long-term operation stability. Such excellent activity and durability were attributed to the synergistic SMSI of the single atomic sites of W and Co in the W-CoOOH-TT pair sites catalyst.<sup>[44]</sup>

The W-CoOOH-TT-1000 pair sites catalyst only required the overpotential as low as 400 and 450 mV to achieve ultra-high current density of 1,000 and 1,760 mA cm<sup>-2</sup> with the *iR* correction (Figure 3e), respectively. We further examined the water oxidation performance of other catalysts (W-CoOOH-TT, reported Ru/NiFe-LDH, and W/CoOOH) and discovered that W-CoOOH-TT-1000 unexpectedly exhibited the highest oxidation current peaks (Figure 3e and Figures S44–S46,

Supporting Information). The intrinsic activities of the W-CoOOH-TT-1000 pair sites catalysts and controls were further determined by calculating the electrochemically active surface area (ECSA). The W-CoOOH-TT-1000 demonstrated high current density of  $1.2 \text{ mA cm}^{-2}_{\text{ECSA}}$  at overpotential of 370 mV, which was  $\sim 30$  and  $240$  times larger than those of CoCuFeAgMoOOH ( $0.04 \text{ mA cm}^{-2}_{\text{ECSA}}$ ) and CoOOH ( $0.005 \text{ mA cm}^{-2}_{\text{ECSA}}$ ),<sup>[55, 56]</sup> respectively, and even exceeded that of most reported materials (Figure S47, Supporting Information). In addition, the comparison of the water oxidation activity results demonstrated that the W-CoOOH-TT-1000 catalyst only required low overpotential to drive  $10 \text{ mA cm}^{-2}$  current density and outperformed various types of previously reported catalysts (Figure 3f) and was thus the state-of-the-art Co-based catalyst for achieving ultrahigh-current-density water oxidation (Figure S48 and Table S8, Supporting Information). The superior catalytic activity primarily originated from the synergy of highly active Co(oxyhydr)-oxides supported atomically dispersed tungsten sites and Co sites through SMSI during the OER cycling,<sup>[57]</sup> which could greatly promote the charge transfer and effectively activated water-oxidation reaction kinetics and increase the possibility of its practical applications. For rationally designing a well-matched electrode to pair with a low cell voltage toward industrial water-splitting applications, MoNi<sub>4</sub> with better hydrogen evolution reaction (HER) activity was selected as the cathode catalyst (Figures S49 and S50, Supporting Information). In the experiment, the water–alkali electrolyzer for efficient hydrogen production can be driven by photovoltaic-electrocatalysis (PV-EC) technology using a commercial Si solar panel under natural sunlight (Figure S51, Supporting Information). To further evaluate the practical value of the catalyst, we assembled an overall water splitting device to test the long-term stability under a high-concentration electrolyte of 6.0-M KOH (Figure S52, Supporting Information).

The results suggested superior sustainability for hydrogen production from water splitting over 1,000 h of continuous operation.

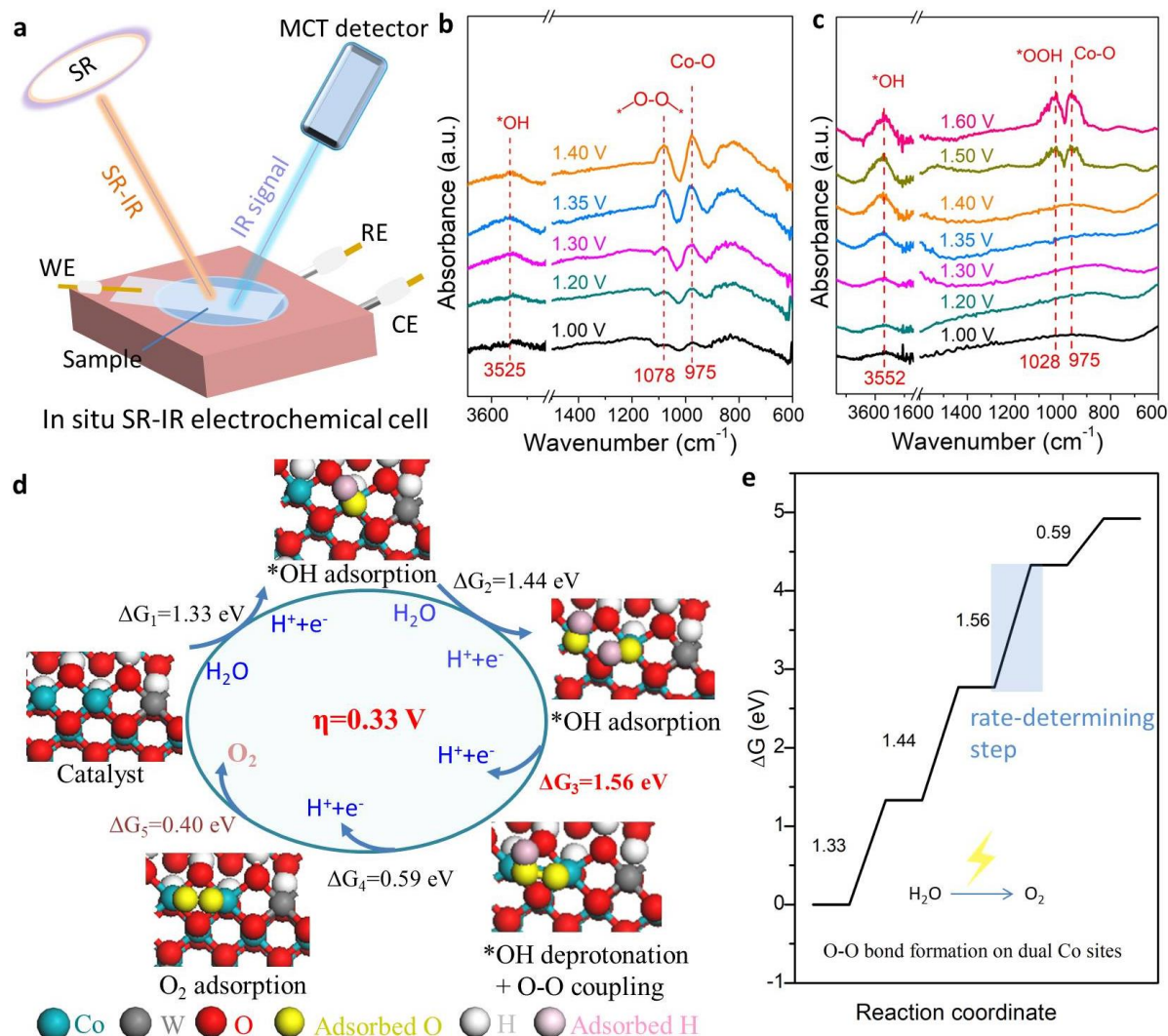


**Figure 4.** In situ SR-FTIR spectroscopy and theoretical investigations into OER catalytic mechanism. a) Schematic illustrations of in situ SR-FTIR electrochemical cell set-up. CE, counter electrode; RE, reference electrode; WE, working electrode. b,c) In situ SR-FTIR characterizations in different potentials (vs. RHE) for the W-CoOOH-TT pair sites via in situ topology transformation of W-Co<sub>9</sub>S<sub>8</sub> (b) and CoOOH via in situ topology transformation of Co<sub>9</sub>S<sub>8</sub> (c) during potential cycling process. d) Gibbs free energy diagram of water oxidation reaction over top views of W-CoOOH-TT pair sites catalyst with a linear Co-Co-W configuration. The schematic models of the key steps and intermediates were exhibited, as well as the energy barriers between the corresponding crucial steps. e) Gibbs free energy ( $\Delta G$ ) diagram for the four electron transfer steps.

This article is protected by copyright. All rights reserved.

**Dual-site mechanism insights into the OER combined with in situ SR-FTIR study and DFT calculation.**

To further probe the OER catalytic mechanism, the in situ SR-FTIR measurements were performed.<sup>[31, 58]</sup> The tests were conducted using a home-made infrared (IR) reflection cell.<sup>[58, 59]</sup> Figure 4a presents the schematic of the electrochemical cell set-up with in situ SR-FTIR spectroscopy. The IR signal revealed an obvious absorption band at 975 and 1,078  $\text{cm}^{-1}$  during the topological transformation process from  $\text{W-Co}_9\text{S}_8$  to the  $\text{W-CoOOH-TT}$  pair-site catalyst with the potential increasing in the range of 1.00–1.40 V vs. RHE, as shown in Figure 4b. It should be noted that the peak intensity at 975  $\text{cm}^{-1}$  gradually increased as the voltage increased, thus suggesting a potential-dependent relationship and the emergence of an obvious structural change during the OER. Based on the feature IR vibration signals of the cobalt/oxygen stretching modes, we attributed the band at approximately 975  $\text{cm}^{-1}$  to the emergence of Co-O species during the OER,<sup>[60, 61]</sup> but not to chemically adsorbed OOH radicals.<sup>[31, 62]</sup> This was consistent with the above series of in situ XAFS experimental results obtained: enhanced voltage driving and single atomic site W loading accelerated the conversion of  $\text{Co}_9\text{S}_8$  to  $\text{CoOOH}$  and also promoted the conversion of oxygenated species in the OER. Moreover, an obvious absorption band at an approximate vibration frequency of 1,078  $\text{cm}^{-1}$  further confirmed the O–O bond formation mechanism, which usually indicated the formation of oxygen bridges between the metal sites in the OPM-type OER mechanism and was consistent with previous reports.<sup>[26, 33–35]</sup> Accordingly, the peak intensity increased as the potential was increased from 1.00 to 1.40 volts vs. RHE. Moreover, a new absorption band was observed at approximately 3,525  $\text{cm}^{-1}$  and could be assigned to the stretching mode of the hydroxyl radicals ( $^*\text{OH}$ ) derived from adsorbed water molecules (Figure 4b), and the intensity of this band increased gradually as the potential increased from 1.00 to 1.30 V vs. RHE. We successfully observed the

potential-dependent characteristic peak of  $3,525\text{ cm}^{-1}$ , which was also consistent with the calculated vibrational frequencies and previous reports.<sup>[26, 59, 61]</sup> This result indicated an evident accumulation of adsorbed O–H of the catalysts under the OER conditions. Furthermore, we could clearly observe that, when the potential exceeded 1.30 V vs. RHE, the signal intensity of the  $^*\text{OH}$  species did not increase obviously with the increase in potential, which was mainly owing to the rapid oxygen–oxygen coupling of the  $^*\text{OH}$  species adsorbed on the double Co sites to obtain oxygen bridges at this time. The above results provide solid experimental evidence for our W-CoOOH-TT pair-site catalysts with a linear Co–Co–W configuration following the two-site OPM-type OER mechanism. The in situ measurements that probed the characteristic changes in the reaction intermediates and surface chemistry of the W-CoOOH-TT pair sites catalysts indicated that the OER followed an OPM-type mechanism without the formation of metal- $^*\text{OOH}$ . However, the in situ SR-FTIR demonstrated that the signal of CoOOH derived from  $\text{Co}_9\text{S}_8$  appeared an obvious absorption band at  $1028\text{ cm}^{-1}$  as the potential increase over 1.40 V vs. RHE (Figure 4c) revealed the emergence of the strong adsorption of superoxide  $^*\text{OOH}$  species over the single Co sites and provided evidence that  $\text{Co}_9\text{S}_8$  follows the adsorbate evolution mechanism (AEM) single-site reaction pathway.<sup>[31, 62, 63]</sup> This may be because bare  $\text{Co}_9\text{S}_8$  cannot be converted into favorable pair sites following the OPM of direct oxygen evolution without the existence of high-valence single-atom metal species.<sup>[44]</sup> Moreover, the characteristic peak (O–O) belonging to OPM-type was not detected in the case of  $\text{Co}_9\text{S}_8$  even at high potentials ( $\geq 1.50\text{ V}$  vs. RHE). To deeply elucidate the relationship between the existence of Co–O species and the accumulation of key O–O species, the gradually enhanced peak intensities of the absorption bands at  $975$  and  $1,078\text{ cm}^{-1}$  were both expressed as a function of the various applied potentials, as displayed in Figure S53 (Supporting Information). Careful observation revealed that

CoOOH was preferentially generated on the surface of W-Co<sub>9</sub>S<sub>8</sub> SACs compared to Co<sub>9</sub>S<sub>8</sub>, which is attributed to the SMSI with charge transfer between the single-atomic-site W and Co<sub>9</sub>S<sub>8</sub> supports and the gradually increasing potential. Consequently, the synergy of the atomically dispersed tungsten and topochemical self-reconstruction of the CoOOH species accelerated the conversion of oxygen-containing intermediates and contributed to easy O-O coupling at a lower potential.<sup>[32]</sup>

To gain further insight into the origin of this superior OER activity, first-principles calculations were performed to elucidate the mechanism underlying the catalytic process. In the DFT simulations, we mainly considered various potential models, including conventional single-site and favorable dual-site models (Figures S54–S58 and Table S9, Supporting Information). When considering the single site in W-CoOOH-TT pair sites catalysts, the free energy of the rate-determining step (RDS) was relatively large as 1.14 eV (Figure S54, Supporting Information). This is inconsistent with our excellent experimental results. Inspired by the dual metal sites in CoO<sub>x</sub>(OH)<sub>y</sub>,<sup>[31, 32]</sup> we also probed a potential dual-metal-site mechanism in W-CoOOH-TT pair sites catalysts with a linear Co-Co-W configuration. The Figure 4d and Figure S55 (Supporting Information) presented the mechanism cycles of double Co active sites for water oxidation on pair sites model with a linear Co–Co–W configuration. Furthermore, the addition of an atomically dispersed W dopant in the vicinity of the Co active sites in CoOOH facilitated the O–O coupling process and evidently dropped the overpotential of RDS for the O–O bond formation in the OER. As a result, the W-CoOOH-TT pair sites had optimal intermediate adsorption free energy and only required a low theoretical OER overpotential of 0.33 V for the RDS (Figure 4d and 4e), which was even lower than that of the state-of-the-art G-FeCoW (0.40 V).<sup>[9]</sup> An in-depth study also found that, in the case of a linear Co–Co–W configuration with dual Co metal sites, the intermediates of \*OH on the two suitable Co site

distances achieved rapid O–O coupling in the presence of a single-atom W site under the influence of SMSI (Figures S55–S57, Supporting Information). Furthermore, the calculated transition state energy of the above O–O bond formation process in this system was consistent with the previously reported two site OER process.<sup>[27, 29, 32]</sup> As compared with the optimal pair-site model in five-coordination W species (Figure S55, Supporting Information), the OH<sup>−</sup> adsorption at the continuous Co sites of the six-coordinated W model was too difficult to achieve for realizing the transformation from OH<sup>−</sup> to the next intermediate \*OH in view of decreasing the coverage (Figure S58, Supporting Information), which resulted in a higher energy barrier for  $\Delta G_1$  and  $\Delta G_2$ .<sup>[52, 64]</sup> The linear Co–Co–W configuration of the W-CoOOH-TT pair sites was the most beneficial and reasonable for the deprotonation of \*OH, and further oxygen–oxygen coupling processes occurred at the two-site cobalt through oxygen bridges for the following OPM-type OER mechanism as compared with other models. Moreover, the simulated O–O vibrational frequencies for the di- $\mu$ -oxo bridges configuration was 1085 cm<sup>−1</sup> as obtained from the DFT calculation, which was consistent with the in situ XAFS results, in situ SR-FTIR results, and previous reports.<sup>[26, 35]</sup> Based on the in situ SR-FTIR and theoretical calculations, we drew the reasonable conclusion that the dual metal Co-site OPM-type for clear O–O bond formation in water oxidation was more suitable for the pair site system than the traditional single site system (Figure S59, Supporting Information), which broke the conventional single-site process. Furthermore, the dual-site water-oxidation mechanism that we raised and confirmed clearly indicated that the true active center of the W-CoOOH-TT pair-site catalyst were the adjacent double Co sites tuned by atomically dispersed W. Such a plausible and favorable catalytic mechanism of single-atomic-site W-tuned dual Co sites was mainly based on the following analysis: 1) single-atomic-site tungsten played a vital role in facilitating dynamic CoOOH active-site generation via



topochemical transformation and easily achieving O–O coupling at lower potentials through the SMSI effect; 2) the SMSI effect with changes in the geometric and electronic structure via high-valence atomically dispersed W at the surrounding Co sites (Figures S60–S62, Supporting Information).<sup>[9]</sup>

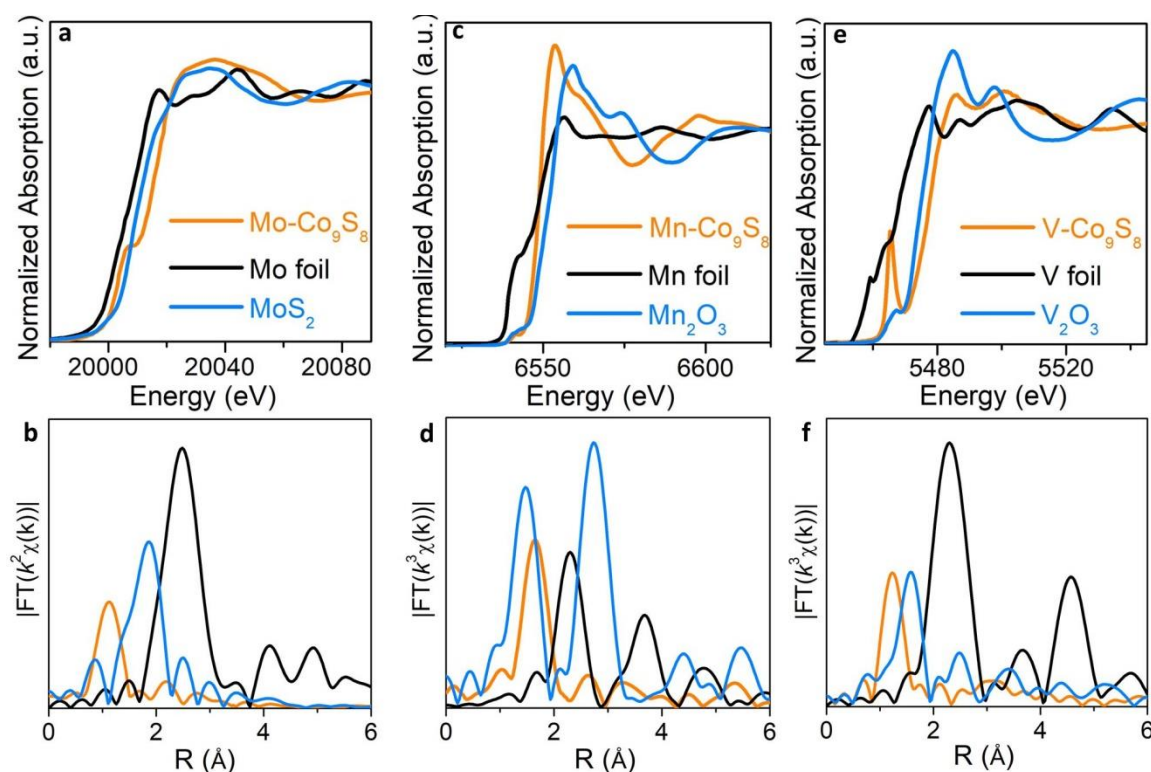


**Figure 5.** The experimental K-edge XANES and FT-EXAFS spectra of a,b) Mo-Co<sub>9</sub>S<sub>8</sub> and reference samples (MoS<sub>2</sub> and Mo foil), and c,d) Mn-Co<sub>9</sub>S<sub>8</sub> and reference samples (Mn<sub>2</sub>O<sub>3</sub> and Mn foil), and e,f) The experimental FT-EXAFS spectra of V-Co<sub>9</sub>S<sub>8</sub> and reference samples (V<sub>2</sub>O<sub>3</sub> and V foil).

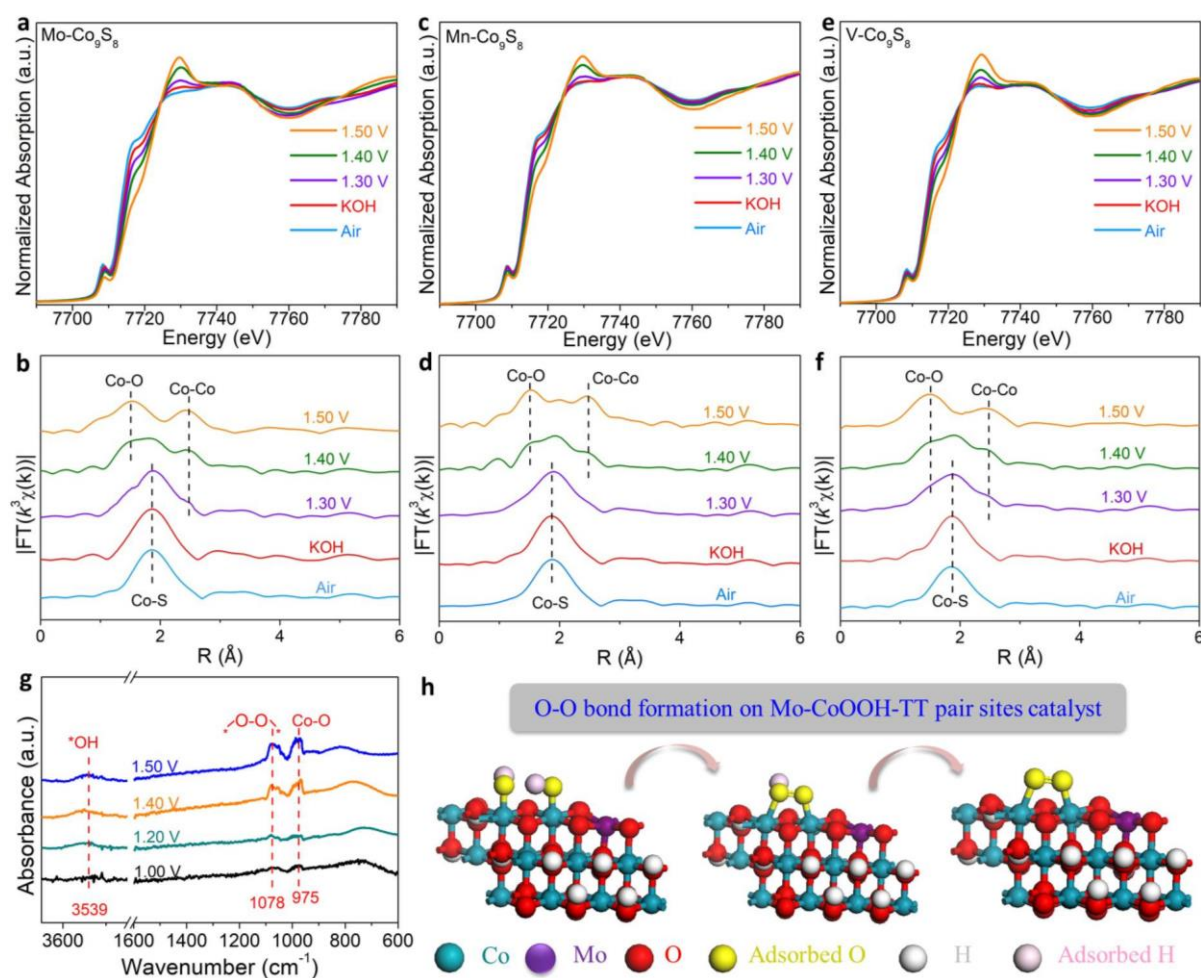


**Figure 6.** In situ Co  $K$ -edge XANES and the Fourier-transformed  $k^3$ -weighted EXAFS spectra of a,b) Mo-Co<sub>9</sub>S<sub>8</sub>, c,d) Mn-Co<sub>9</sub>S<sub>8</sub>, and e,f) V-Co<sub>9</sub>S<sub>8</sub> SACs with structural topochemical transformation during potential cycling. g) In situ SR-FTIR signal in the range of 600–3700 cm<sup>-1</sup> under various potentials during topological transformation from Mo-Co<sub>9</sub>S<sub>8</sub> to Mo-CoOOH-TT pair sites catalyst. h) The free-energy diagrams for Mo-CoOOH-TT pair sites catalysts.

**A general effect of atomically dispersed high valence metals for promoting topochemical transformation via potential cycling.** To investigate the versatility of the “PCTT” strategy by converting SACs into pair-sites catalysts, we first prepared various M-Co<sub>9</sub>S<sub>8</sub> (M = Mo, Mn, and V) SACs via similar synthetic procedures by replacing tungsten with other metals (for details, see Methods, Supporting Information). As expected, the EXAFS and XANES results for the M-Co<sub>9</sub>S<sub>8</sub> SACs

(M = Mo, Mn, and V) confirmed that the metal species of Mo, Mn, and V all existed in the form of an atomic dispersion (Figure 5), while no metal–metal bonds were detected. In addition, a series of characterizations, including EDS mapping, XRD with Rietveld refinement, and TEM, were used to fully reveal the composition, structure, and morphology of the Mo-Co<sub>9</sub>S<sub>8</sub>, Mn-Co<sub>9</sub>S<sub>8</sub>, and V-Co<sub>9</sub>S<sub>8</sub> catalysts (Figures S63–S65, Supporting Information). Furthermore, in situ XAFS was also used to reveal the topological transformation process of Co<sub>9</sub>S<sub>8</sub> supports assisted by high-valence monoatomic metals. Similarly, the in situ XAFS results also revealed that the loading of other high-valence metals (Mo, Mn, and V) exhibited a similar trend to that of W, thus promoting the efficient structural transformation from Co<sub>9</sub>S<sub>8</sub> to CoOOH at lower potentials through potential cycling (Figure 6a-f). In addition, the CV characteristic peaks of cobalt oxyhydroxide for loading the high-valence metal (Mo, Mn, V) single atoms were also detected through 30<sup>th</sup> CVs cycling (Figure S66, Supporting Information). This is also proven by the fact that a general effect of atomically dispersed high-valence metals can promote the pre-oxidation of lower-valence Co species and accelerate the subsequent formation of highly stable Co oxyhydroxide via potential cycling, further contributing to the long-term OER stability. Our results were consistent with those of previous studies, demonstrating the promotional effects of W, Mo, Ta, Nb, Ni, and Fe on the OER activity and durability of Co oxides.<sup>[9, 10, 30]</sup> Likewise, according to the “PCTT” strategy of preparing W-CoOOH-TT pair sites catalysts, we cycled M-Co<sub>9</sub>S<sub>8</sub> SACs (M = Mo, V, and Mn) for 900-segment cycling to ensure that Co<sub>9</sub>S<sub>8</sub> can be sufficiently converted into M-CoOOH-TT pair sites catalysts (Figure S67, Supporting Information). In general, the above results of the in situ XAFS, AC HAADF–STEM images, XPS, TEM, HRTEM, HAADF–STEM, and corresponding EDS mapping (Figure 6a-f and Figures S68–S72, Supporting

Information) confirmed that the Mo-CoOOH-TT, V-CoOOH-TT, and Mn-CoOOH-TT pair sites catalysts were constructed via “PCTT” methods.

Furthermore, we used in situ IR to explore the OER mechanism of the above pair sites catalysts. The presence of oxygen bridges between the dual Co metal sites was also observed in the in situ SR-FTIR results of the M-CoOOH-TT (M = Mo, V, and Mn) pair sites catalysts with atomically dispersed high-valence metals Mo, Mn, and V (Figure 6g and Figure S73, Supporting Information). The vibration frequency of  $1,078\text{ cm}^{-1}$  was attributed to the formation of an O–O bond, which was in the same as W-CoOOH-TT pair sites catalyst. The above results provided solid evidence that M-CoOOH-TT (M = Mo, V, and Mn) pair sites catalysts follow a dual-site OPM-type mechanism with O–O bond formation during water oxidation. Moreover, the DFT calculations demonstrated that the Mo-CoOOH-TT pair sites also followed the OPM-type OER (Figure 6h and Figure S74, Supporting Information) and exhibited an obvious oxygen–oxygen coupling process at the dual Co sites with oxygen bridges, which was also consistent with the in situ IR results. Therefore, we reported the general effect of incorporating a high-valence atomically dispersed transition metal for boosting the topochemical transformation under potential cycling to fabricate M-CoOOH-TT (M = W, Mo, Mn, and V) pair-site catalysts, which further followed the direct  $\text{O}_2$  evolution OPM-type OER mechanism.

### 3. Conclusion

In summary, we reported a general “topochemical transformation strategy” for constructing noble-metal-free M-CoOOH-TT pair sites catalysts (M = W, Mo, Mn, and V) via facile potential cycling. We revealed the general rule of the high-valence metal modulating effect for inducing  $\text{Co}_9\text{S}_8$  supports in situ topochemical reconstruction of highly stable pair sites catalysts with suitable cobalt–cobalt distances at the atomic scale through in situ XAFS. We identified a favorable two-site OPM-type

direct O–O bond formation for O<sub>2</sub> evolution that involved the typical forming oxygen bridges between dual-metal Co sites with a distinctive absorption peak at 1,078 cm<sup>-1</sup> via in situ SR-FTIR and DFT simulations, thus breaking the shackles of the traditional single-site electrochemical mechanism. The prepared pair sites catalyst exhibited a record sustainable stability of 1,000 h and near-industrial 1,000 h real-world applications of water splitting. These findings provided design principles for highly efficient, sustainable, noble-metal-free pair sites catalysts, and a plausible two-site direct O<sub>2</sub> evolution mechanism that could aid in solving the bottleneck problem of practical water oxidation.

## Experimental Section

Experimental details are seen in the supporting information.

## Supporting Information

Supporting Information is available from the Wiley Online Library or from the author.

## Acknowledgements

The authors acknowledge support from the National Basic Research Program of China (no. 2020YFA0210700) and National Natural Science Foundation of China (nos. U21A20285, 21871009, and 22125102). Q. L. also acknowledges support from the National Natural Science Foundation of China (grant no. U1932212). X. S. gratefully acknowledges the National Natural Science Foundation of China (no. 21935001), the National Key Research and Development Project (no. 2018YFB1502401). We also gratefully thank the 1W1B beamline at the Beijing Synchrotron Radiation Facility (BSRF), and the BL01B beamline at the National Synchrotron Radiation Laboratory (NSRL), China. **Author contributions:** J.S. and L.W. conceived the idea. L.W. designed and performed the experiments, and analyzed the experimental results. H.S. and Q.L. collected the XAFS, in situ XAFS and SR-FTIR data and helped analyze the experimental results. G.T. and Y.L. carried out the DFT simulations. J.X. and Z.Z. assisted in the electrochemical test. X.D. and H.X. assisted with the discussion of DFT simulations. X.W., J.J. and Y.Q. carried out TEM and HRTEM measurements. H.L., X.L., W.C., D.W. contributed to the discussion of results and gave valuable suggestions. L.W., H.S., G.T., Q.L., X.S. and J.S. analyzed and discussed the experimental results and drafted the manuscript. L.G. Wang, H. Su, G.Y. Tan, and J.J. Xin contributed equally to this work.

## Conflict of Interest

The authors declare no conflict of interest.

Received: ((will be filled in by the editorial staff))

Revised: ((will be filled in by the editorial staff))

Published online: ((will be filled in by the editorial staff))

## Data Availability Statement

The data that support the findings of this study are available from the corresponding author upon reasonable request.

## References

- [1] J. Greeley, T. F. Jaramillo, J. Bonde, I. Chorkendorff, J. K. Nørskov, *Nat. Mater.* **2006**, *5*, 909-913.
- [2] J. N. Tiwari, N. K. Dang, S. Sultan, P. Thangavel, H. Y. Jeong, K. S. Kim, *Nat. Sustain.* **2020**, *3*, 556-563.
- [3] Z. W. Seh, J. Kibsgaard, C. F. Dickens, I. Chorkendorff, J. K. Nørskov, T. F. Jaramillo, *Science* **2017**, *355*, eaad4998.
- [4] M. Li, Z. Zhao, T. Cheng, A. Fortunelli, C.-Y. Chen, R. Yu, Q. Zhang, L. Gu, B. V. Merinov, Z. Lin, E. Zhu, T. Yu, Q. Jia, J. Guo, L. Zhang, W. A. Goddard, Y. Huang, X. Duan, *Science* **2016**, *354*, 1414.
- [5] C. Seitz Linsey, F. Dickens Colin, K. Nishio, Y. Hikita, J. Montoya, A. Doyle, C. Kirk, A. Vojvodic, Y. Hwang Harold, K. Nørskov Jens, F. Jaramillo Thomas, *Science* **2016**, *353*, 1011-1014.
- [6] A. Bhowmick, R. Hussein, I. Bogacz, P. S. Simon, M. Ibrahim, R. Chatterjee, M. D. Doyle, M. H. Cheah, T. Fransson, P. Chernev, I.-S. Kim, H. Makita, M. Dasgupta, C. J. Kaminsky, M. Zhang, J. Gätcke, S. Haupt, I. I. Nangca, S. M. Keable, A. O. Aydin, K. Tono, S. Owada, L. B. Gee, F. D. Fuller, A. Batyuk, R. Alonso-Mori, J. M. Holton, D. W. Paley, N. W. Moriarty, F. Mamedov, P. D. Adams, A. S. Brewster, H. Dobbek, N. K. Sauter, U. Bergmann, A. Zouni, J. Messinger, J. Kern, J. Yano, V. K. Yachandra, *Nature* **2023**, *617*, 629-636.
- [7] M. Blasco-Ahicart, J. Soriano-López, J. J. Carbó, J. M. Poblet, J. R. Galan-Mascaros, *Nat. Chem.* **2018**, *10*, 24-30.
- [8] J. Guan, Z. Duan, F. Zhang, S. D. Kelly, R. Si, M. Dupuis, Q. Huang, J. Q. Chen, C. Tang, C. Li, *Nat. Catal.* **2018**, *1*, 870-877.

This article is protected by copyright. All rights reserved.

- [9] B. Zhang, X. Zheng, O. Voznyy, R. Comin, M. Bajdich, M. García-Melchor, L. Han, J. Xu, M. Liu, L. Zheng, F. P. García de Arquer, C. T. Dinh, F. Fan, M. Yuan, E. Yassitepe, N. Chen, T. Regier, P. Liu, Y. Li, P. De Luna, A. Janmohamed, H. L. Xin, H. Yang, A. Vojvodic, E. H. Sargent, *Science* **2016**, 352, 333.
- [10] B. Zhang, L. Wang, Z. Cao, S. M. Kozlov, F. P. García de Arquer, C. T. Dinh, J. Li, Z. Wang, X. Zheng, L. Zhang, Y. Wen, O. Voznyy, R. Comin, P. De Luna, T. Regier, W. Bi, E. E. Alp, C.-W. Pao, L. Zheng, Y. Hu, Y. Ji, Y. Li, Y. Zhang, L. Cavallo, H. Peng, E. H. Sargent, *Nat. Catal.* **2020**, 3, 985-992.
- [11] P. Liu, Y. Zhao, R. Qin, S. Mo, G. Chen, L. Gu, D. M. Chevrier, P. Zhang, Q. Guo, D. Zang, B. Wu, G. Fu, N. Zheng, *Science* **2016**, 352, 797.
- [12] H. Fei, J. Dong, Y. Feng, C. S. Allen, C. Wan, B. Voloskiy, M. Li, Z. Zhao, Y. Wang, H. Sun, P. An, W. Chen, Z. Guo, C. Lee, D. Chen, I. Shakir, M. Liu, T. Hu, Y. Li, A. I. Kirkland, X. Duan, Y. Huang, *Nat. Catal.* **2018**, 1, 63-72.
- [13] X.-F. Yang, A. Wang, B. Qiao, J. Li, J. Liu, T. Zhang, *Acc. Chem. Res.* **2013**, 46, 1740-1748.
- [14] J. Liu, Q. Hu, Y. Wang, Z. Yang, X. Fan, L.-M. Liu, L. Guo, *Proc. Natl. Acad. Sci. USA* **2020**, 117, 21906.
- [15] S. J. Tauster, *Acc. Chem. Res.* **1987**, 20, 389-394.
- [16] S. J. Tauster, S. C. Fung, R. L. Garten, *J. Am. Chem. Soc.* **1978**, 100, 170-175.
- [17] M. Monai, K. Jenkinson, A. E. M. Melcherts, J. N. Louwen, E. A. Irmak, S. Van Aert, T. Altantzis, C. Vogt, W. van der Stam, T. Duchoň, B. Šmíd, E. Groeneveld, P. Berben, S. Bals, B. M. Weckhuysen, *Science* **2023**, 380, 644-651.
- [18] D. Cao, D. Liu, S. Chen, O. A. Moses, X. Chen, W. Xu, C. Wu, L. Zheng, S. Chu, H. Jiang, C. Wang, B. Ge, X. Wu, J. Zhang, L. Song, *Energy Environ. Sci.* **2021**, 14, 906-915.
- [19] Y. Yang, M. Yuan, H. Li, G. Sun, S. Ma, *Electrochim. Acta* **2018**, 281, 198-207.
- [20] Z. Du, S. Yang, S. Li, J. Lou, S. Zhang, S. Wang, B. Li, Y. Gong, L. Song, X. Zou, P. M. Ajayan, *Nature* **2020**, 577, 492-496.
- [21] Y. Deng, X. Xi, Y. Xia, Y. Cao, S. Xue, S. Wan, A. Dong, D. Yang, *Adv. Mater.* **2022**, 34, 2109145.
- [22] I. Ro, J. Qi, S. Lee, M. Xu, X. Yan, Z. Xie, G. Zakem, A. Morales, J. G. Chen, X. Pan, D. G. Vlachos, S. Caratzoulas, P. Christopher, *Nature* **2022**, 609, 287-292.
- [23] R. Gao, J. Wang, Z.-F. Huang, R. Zhang, W. Wang, L. Pan, J. Zhang, W. Zhu, X. Zhang, C. Shi, J. Lim, J.-J. Zou, *Nat. Energy* **2021**, 6, 614-623.

- [24] X. Zheng, J. Yang, Z. Xu, Q. Wang, J. Wu, E. Zhang, S. Dou, W. Sun, D. Wang, Y. Li, *Angew. Chem. Int. Ed.* **2022**, *61*, e202205946.
- [25] D. W. Shaffer, Y. Xie, J. J. Concepcion, *Chem. Soc. Rev.* **2017**, *46*, 6170-6193.
- [26] C. Lin, J.-L. Li, X. Li, S. Yang, W. Luo, Y. Zhang, S.-H. Kim, D.-H. Kim, S. S. Shinde, Y.-F. Li, Z.-P. Liu, Z. Jiang, J.-H. Lee, *Nat. Catal.* **2021**, *4*, 1012-1023.
- [27] H. Xiao, H. Shin, W. A. Goddard, *Proc. Natl. Acad. Sci. USA* **2018**, *115*, 5872-5877.
- [28] H. Shin, H. Xiao, W. A. Goddard, *J. Am. Chem. Soc.* **2018**, *140*, 6745-6748.
- [29] B. Tian, H. Shin, S. Liu, M. Fei, Z. Mu, C. Liu, Y. Pan, Y. Sun, W. A. Goddard Iii, M. Ding, *Angew. Chem. Int. Ed.* **2021**, *60*, 16448-16456.
- [30] L. Bai, C.-S. Hsu, D. T. L. Alexander, H. M. Chen, X. Hu, *Nat. Energy* **2021**, *6*, 1054-1066.
- [31] M. Zhang, M. de Respinis, H. Frei, *Nat. Chem.* **2014**, *6*, 362-367.
- [32] C. Lang, J. Li, K. R. Yang, Y. Wang, D. He, J. E. Thorne, S. Croslow, Q. Dong, Y. Zhao, G. Prostko, G. W. Brudvig, V. S. Batista, M. M. Waagele, D. Wang, *Chem* **2021**, *7*, 2101-2117.
- [33] T. Shibahara, M. Mori, *Bull. Chem. Soc. Jpn* **1978**, *51*, 1374-1379.
- [34] Y. Zhang, H. Zhang, A. Liu, C. Chen, W. Song, J. Zhao, *J. Am. Chem. Soc.* **2018**, *140*, 3264-3269.
- [35] B. Wang, K. Zhao, Z. Yu, C. Sun, Z. Wang, N. Feng, L. Mai, Y. Wang, Y. Xia, *Energy Environ. Sci.* **2020**, *13*, 2200-2208.
- [36] E. Fabbri, M. Nachtegaal, T. Binninger, X. Cheng, B.-J. Kim, J. Durst, F. Bozza, T. Graule, R. Schäublin, L. Wiles, M. Pertoso, N. Danilovic, K. E. Ayers, T. J. Schmidt, *Nat. Mater.* **2017**, *16*, 925-931.
- [37] J. Yan, L. Kong, Y. Ji, J. White, Y. Li, J. Zhang, P. An, S. Liu, S.-T. Lee, T. Ma, *Nat. Commun.* **2019**, *10*, 2149.
- [38] Y. Feng, C. Wang, P. Cui, C. Li, B. Zhang, L. Gan, S. Zhang, X. Zhang, X. Zhou, Z. Sun, K. Wang, Y. Duan, H. Li, K. Zhou, H. Huang, A. Li, C. Zhuang, L. Wang, Z. Zhang, X. Han, *Adv. Mater.* **2022**, *34*, 2109074.
- [39] C.-J. Chen, C.-Y. Yeh, C.-H. Chen, A. Jena, D.-H. Wei, H. Chang, S.-F. Hu, R.-S. Liu, *ACS Appl. Mater. Interfaces* **2020**, *12*, 54671-54682.
- [40] A. Moysiadou, S. Lee, C.-S. Hsu, H. M. Chen, X. Hu, *J. Am. Chem. Soc.* **2020**, *142*, 11901-11914.



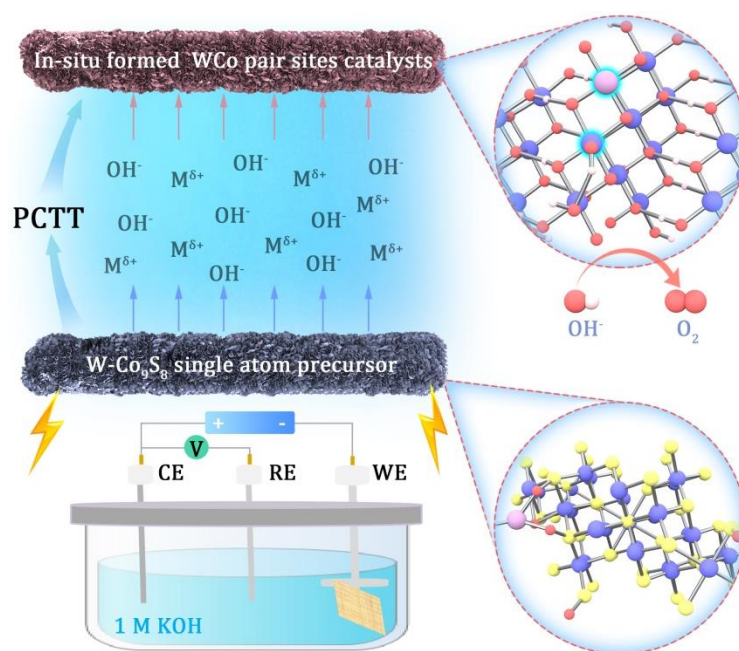
- [41] A. Bergmann, T. E. Jones, E. Martinez Moreno, D. Teschner, P. Chernev, M. Gliech, T. Reier, H. Dau, P. Strasser, *Nat. Catal.* **2018**, *1*, 711-719.
- [42] F. T. Haase, A. Bergmann, T. E. Jones, J. Timoshenko, A. Herzog, H. S. Jeon, C. Rettenmaier, B. R. Cuenya, *Nat. Energy* **2022**, *7*, 765-773.
- [43] M. W. Kanan, J. Yano, Y. Surendranath, M. Dincă, V. K. Yachandra, D. G. Nocera, *J. Am. Chem. Soc.* **2010**, *132*, 13692-13701.
- [44] T. Wu, S. Sun, J. Song, S. Xi, Y. Du, B. Chen, W. A. Sasangka, H. Liao, C. L. Gan, G. G. Scherer, L. Zeng, H. Wang, H. Li, A. Grimaud, Z. J. Xu, *Nat. Catal.* **2019**, *2*, 763-772.
- [45] J. Xu, Q. Wang, X. Wang, Q. Xiang, B. Liang, D. Chen, G. Shen, *ACS Nano* **2013**, *7*, 5453-5462.
- [46] J. Zhou, Y. Wang, X. Su, S. Gu, R. Liu, Y. Huang, S. Yan, J. Li, S. Zhang, *Energy Environ. Sci.* **2019**, *12*, 739-746.
- [47] H. Zhou, Z. Li, S.-M. Xu, L. Lu, M. Xu, K. Ji, R. Ge, Y. Yan, L. Ma, X. Kong, L. Zheng, H. Duan, *Angew. Chem. Int. Ed.* **2021**, *60*, 8976-8982.
- [48] Q.-L. Hong, Q.-G. Zhai, X.-L. Liang, Y. Yang, F.-M. Li, Y.-C. Jiang, M.-C. Hu, S.-N. Li, Y. Chen, *J. Mater. Chem. A* **2021**, *9*, 3297-3302.
- [49] N. Yao, G. Wang, H. Jia, J. Yin, H. Cong, S. Chen, W. Luo, *Angew. Chem. Int. Ed.* **2022**, *61*, e202117178.
- [50] K. Fan, H. Zou, Y. Lu, H. Chen, F. Li, J. Liu, L. Sun, L. Tong, M. F. Toney, M. Sui, J. Yu, *ACS Nano* **2018**, *12*, 12369-12379.
- [51] J. T. Mefford, A. R. Akbashev, M. Kang, C. L. Bentley, W. E. Gent, H. D. Deng, D. H. Alsem, Y.-S. Yu, N. J. Salmon, D. A. Shapiro, P. R. Unwin, W. C. Chueh, *Nature* **2021**, *593*, 67-73.
- [52] S. Zhao, C. Tan, C.-T. He, P. An, F. Xie, S. Jiang, Y. Zhu, K.-H. Wu, B. Zhang, H. Li, J. Zhang, Y. Chen, S. Liu, J. Dong, Z. Tang, *Nat. Energy* **2020**, *5*, 881-890.
- [53] J. Liu, Q. Hu, Y. Wang, Z. Yang, X. Fan, L.-M. Liu, L. Guo, *Proc. Natl. Acad. Sci. USA* **2020**, *117*, 21906-21913.
- [54] A. Grimaud, A. Demortière, M. Saubanière, W. Dachraoui, M. Duchamp, M.-L. Doublet, J.-M. Tarascon, *Nat. Energy* **2016**, *2*, 16189.
- [55] L. Zhang, W. Cai, N. Bao, H. Yang, *Adv. Mater.* **2022**, *34*, 2110511.
- [56] S. Ye, J. Wang, J. Hu, Z. Chen, L. Zheng, Y. Fu, Y. Lei, X. Ren, C. He, Q. Zhang, J. Liu, *ACS Catal.* **2021**, *11*, 6104-6112.

- [57] K. Xu, H. Cheng, L. Liu, H. Lv, X. Wu, C. Wu, Y. Xie, *Nano Lett.* **2017**, *17*, 578-583.
- [58] W. Cheng, X. Zhao, H. Su, F. Tang, W. Che, H. Zhang, Q. Liu, *Nat. Energy* **2019**, *4*, 115-122.
- [59] H. Su, W. Zhou, H. Zhang, W. Zhou, X. Zhao, Y. Li, M. Liu, W. Cheng, Q. Liu, *J. Am. Chem. Soc.* **2020**, *142*, 12306-12313.
- [60] O. Zandi, T. W. Hamann, *Nat. Chem.* **2016**, *8*, 778-783.
- [61] W. Zhou, H. Su, Z. Wang, F. Yu, W. Wang, X. Chen, Q. Liu, *J. Mater. Chem. A* **2021**, *9*, 1127-1133.
- [62] L. Zeng, Z. Zhao, F. Lv, Z. Xia, S.-Y. Lu, J. Li, K. Sun, K. Wang, Y. Sun, Q. Huang, Y. Chen, Q. Zhang, L. Gu, G. Lu, S. Guo, *Nat. Commun.* **2022**, *13*, 3822.
- [63] S. Maintz, V. L. Deringer, A. L. Tchougréeff, R. Dronskowski, *J. Comput. Chem.* **2016**, *37*, 1030-1035.
- [64] Z.-P. Wu, H. Zhang, S. Zuo, Y. Wang, S. L. Zhang, J. Zhang, S.-Q. Zang, X. W. Lou, *Adv. Mater.* **2021**, *33*, 2103004.

# Boosting Efficient and Sustainable Alkaline Water Oxidation on W-CoOOH-TT Pair Sites Catalyst Synthesized via Topochemical Transformation

Ligang Wang, Hui Su, Guoying Tan, Junjie Xin, Xiaoge Wang, Zhuang Zhang, Yaping Li, Yi Qiu, Xiaohui Li, Haisheng Li, Jing Ju, Xinxuan Duan, Hai Xiao, Wenxing Chen, Qinghua Liu\*, Xiaoming Sun\*, Dingsheng Wang and Junliang Sun\*

## Entry for the Table of Contents



A general potential cycling topochemical transformation ("PCTT") strategy was firstly used to convert M-Co<sub>9</sub>S<sub>8</sub> single atom catalysts (SACs) into M-CoOOH-TT pair sites (M=W, Mo, Mn, V) under the modulating of atomically dispersed high valence metals, this TT process can be confirmed by in-situ XAFS. The prepared tungsten based pair sites catalyst made a breakthrough of 3000 mA cm<sup>-2</sup> high current density and 1,000 hours long-term stability. Furthermore, the O-O bond formation

This article is protected by copyright. All rights reserved.

mechanism on two site supporting by in-situ synchrotron radiation infrared and DFT, which breaks the limit of adsorption–energy scaling relationship on conventional single-site.